A Physics-Informed Neural Network Approach to the Point Defect Model for Electrochemical Oxide Film Growth

Mohid Farooqi
Department of Physics and Astronomy
University of Waterloo
Waterloo, Canada

Ingmar Bösing
Chemical Process Engineering (CVT)
University of Bremen
Bremen, Germany

Conrard G. Tetsassi Feugmo
Department of Chemistry
University of Waterloo
Waterloo, Canada
cgtetsas@uwaterloo.ca

Abstract

Physics-informed neural networks (PINNs) offer a novel AI-driven framework for integrating physical laws directly into neural network models, facilitating the solution of complex multiphysics problems in materials engineering. This study systematically explores the application of PINNs to simulate oxide film layer growth in halide-free solutions using the point defect model (PDM). We identify and analyze four key failure modes in this context: imbalanced loss components across different physical processes, numerical instabilities due to variable scale disparities, challenges in enforcing boundary conditions within multiphysics systems, and convergence to mathematically valid but physically meaningless solutions. To overcome these challenges, we implement and validate established techniques including nondimensionalization for training stabilization, Neural Tangent Kernel-based adaptive loss balancing, robust enforcement of boundary conditions and hybrid training with sparse data. Our results demonstrate the effectiveness of these strategies in enhancing the reliability and physical fidelity of PINNs, achieving sub 1% relative error as compared to Finite Element Benchmarks with the hybrid model. This investigation demonstrates that PINNs are capable of conducting high-fidelity electrochemical simulations with minimal data requirements and elucidates the essential factors for achieving fully autonomous PINN simulations.
.

1 Introduction

Material degradation from corrosion represents one of the most significant challenges in engineering, with annual global costs exceeding trillions of dollars [1, 2]. Central to mitigating corrosion is the formation of protective oxide films on metal surfaces, a passivation process that preserves material integrity and underpins performance in applications ranging from biomedical implants to nuclear reactor components [3, 4, 5]. Understanding and predicting oxide film growth requires solving complex multiphysics problems involving coupled transport, electrostatics, and electrochemical reactions at evolving interfaces.

The Point Defect Model (PDM), originally developed by Macdonald and colleagues [6], provides the most comprehensive theoretical framework for electrochemical oxide film growth in halide-free

environments. The model describes film evolution through the generation, transport, and annihilation of point defects—cation vacancies, anion vacancies, and metal interstitials—driven by electric fields and concentration gradients [7, 8]. This multiphysics system requires solving coupled Nernst–Planck equations for ion transport, Poisson's equation for electrostatics, while simultaneously accounting for Butler–Volmer kinetics at moving boundaries [9, 10].

Traditional numerical approaches, particularly finite element methods, have been successfully applied to the PDM [11, 12, 13]. However, these methods face fundamental limitations: mesh regeneration for moving boundaries increases computational cost, parameter studies require complete re-simulation for each parameter set, and inverse problems for parameter estimation remain challenging. Moreover, commercial multiphysics software often functions as a "black box," limiting accessibility and interpretability.

Recently, physics-informed neural networks (PINNs) have emerged as a promising alternative, embedding governing physical laws directly into neural network loss functions [14, 15]. PINNs offer several advantages including mesh-free computation, rapid inference for parameter studies after training, and inherent inverse problem capabilities [13]. Recent successes include voltammetric simulations achieving excellent agreement with analytical solutions [16], hydrodynamic voltammetry capturing complex flow effects [17], and phase field modeling with adaptive weighting strategies [18].

However, applying PINNs to stiff, nonlinear, coupled multiphysics problems like the PDM reveals significant challenges that have limited practical adoption [19]. Through systematic investigation, we identify four primary pathologies: (1) imbalanced loss components between different physics spanning multiple orders of magnitude, (2) numerical instabilities from scale disparities across variables ranging from nanometers to volts, (3) difficulty enforcing boundary conditions in multiphysics systems with moving interfaces, and (4) convergence to mathematically valid but physically meaningless solutions.

This work presents comprehensive solutions to these challenges, demonstrating that properly engineered PINNs can successfully simulate oxide film growth. Our key contributions include: systematic identification of failure modes specific to electrochemical systems, physics-based nondimensionalization extending temporal stability by 250×, Neural Tangent Kernel-based adaptive loss balancing eliminating manual tuning, and diagnostic tools for identifying and resolving convergence issues. We provide actionable guidelines for the broader materials science community to deploy PINNs for complex interfacial phenomena.

2 Point Defect Model Framework

The Point Defect Model describes oxide film growth through the transport and reaction of point defects within a growing oxide layer. We adopt the Refined PDM (R-PDM) formulation by Bösing et al. [9], which explicitly solves the Poisson equation for electric potential. For our PINN implementation, we focus on cation vacancies ($V_{\mathrm{Fe}}^{8/3-}$) and anion vacancies ($V_{\dot{\mathrm{O}}}$) as the primary charge carriers.

2.1 Interfacial Reactions

The main reactions for iron passivation in halide-free solution occur at two interfaces:

At the metal/film (m/f) interface:

- **R1:** $\mathrm{Fe} + \mathrm{V}_{\mathrm{Fe}}^{8/3-} \longrightarrow \mathrm{Fe}_{\mathrm{ox}} + \nu_{\mathrm{Fe}} + 8\frac{}{3}\,\mathrm{e}^-$ (Cation vacancy consumption)
- **R2:** $\mathrm{Fe} \longrightarrow \mathrm{Fe}_{\mathrm{ox}} + \frac{4}{3}\,\mathrm{V}_{\mathrm{O}}^{\bullet} + \frac{8}{3}\,\mathrm{e}^-$ (Anion vacancy production)

At the film/solution (f/s) interface:

- **R3:** $\mathrm{Fe}_{\mathrm{ox}} \longrightarrow \mathrm{Fe}^{3+} + \mathrm{V}_{\mathrm{Fe}}^{8/3-} + \frac{1}{3}\,\mathrm{e}^-$ (Cation vacancy production)
- **R4:** $\mathrm{V}_{\mathrm{O}}^{\bullet} + \mathrm{H}_2\mathrm{O} \longrightarrow \mathrm{O}_{\mathrm{ox}} + \mathrm{H}^+$ (Anion vacancy consumption)
- **R5:** $\mathrm{Fe}_3\mathrm{O}_4 + 8\,\mathrm{H}^+ \longrightarrow 2\,\mathrm{Fe}^{3+} + 4\,\mathrm{H}_2\mathrm{O}$ (Chemical dissolution)

2.2 Governing Equations

The oxide film occupies a time-dependent domain $\Omega(t) = [0, L(t)]$, where $L(t)$ represents the evolving film thickness. Within this domain, defect transport is governed by the Nernst–Planck equation for each species i:

$$\frac{\partial C_i}{\partial t} = -\nabla \cdot \mathbf{J}_i, \quad \mathbf{J}_i = -D_i \nabla C_i - \frac{z_i F D_i C_i}{RT} \nabla \phi, \tag{1}$$

where C_i is concentration, D_i diffusion coefficient, z_i charge number, F Faraday constant, R gas constant, T temperature, and ϕ electrostatic potential. The flux $\mathbf{J}_i$ includes both diffusive and electromigration contributions.

The electric potential distribution satisfies Poisson's equation:

$$-\nabla \cdot (\epsilon \nabla \phi) = F \sum_i z_i C_i, \tag{2}$$

where ϵ is the dielectric permittivity of the oxide.

Interfacial reaction kinetics follow Butler–Volmer form:

$$k_j = k_j^\circ \exp\left(-\alpha_j \frac{F}{RT} \eta_j\right), \tag{3}$$

where k_j° is the exchange rate constant, α_j the transfer coefficient, and $\eta_j = E - E^\circ$ the overpotential for reaction j.

The film thickness evolution is determined by the net rate of non-lattice conserving reactions:

$$\frac{dL}{dt} = \Omega \sum_j \nu_j k_j, \tag{4}$$

where Ω is the molar volume of oxide and ν_j the stoichiometric coefficient for reaction j.

3 Methodology

3.1 PINN Architecture for Multiphysics Modeling

Given the multiphysics nature of the PDM, we employ a segregated PINN architecture where each physical field is represented by a dedicated neural network. This approach, demonstrated superior to single-network formulations by Sun et al. [20], allows each network to specialize in learning specific physics:

- $\mathcal{U}_\phi(x, t, E)$: Electric potential network
- $\mathcal{U}_{CV}(x, t, E)$: Cation vacancy concentration network
- $\mathcal{U}_{AV}(x, t, E)$: Anion vacancy concentration network
- $\mathcal{U}_L(t, E)$: Film thickness evolution network

The moving boundary is explicitly captured through $\mathcal{U}_L$, following Kathane and Karagadde [21]. Each network uses feed-forward architecture with 5 hidden layers of 20 neurons, employing the Swish activation function which yields improved convergence over tanh [22]. The film thickness network excludes spatial input x since thickness depends only on time and applied potential.

3.2 Loss Function Design

The PDM physics is enforced through a composite loss function with four components:

$$\mathcal{L}_{\text{interior}} = \sum_j \frac{1}{N_{\text{int}}} \sum_{i=1}^{N_{\text{int}}} \left| \mathcal{N}_j(\mathcal{U}_j(x_i, t_i)) - \frac{\partial \mathcal{U}_j(x_i, t_i)}{\partial t} \right|^2, \tag{5}$$

$$\mathcal{L}_{\text{boundary}} = \sum_j \frac{1}{N_{\text{bc}}} \sum_{i=1}^{N_{\text{bc}}} \left| \partial\Omega_j(\mathcal{U}_j(x_i, t_i)) \right|^2, \tag{6}$$

$$\mathcal{L}_{\text{initial}} = \sum_j \frac{1}{N_{\text{ic}}} \sum_{i=1}^{N_{\text{ic}}} \left| \mathcal{I}_j(\mathcal{U}_j(x_i)) \right|^2, \tag{7}$$

$$\mathcal{L}_{\text{film}} = \frac{1}{N_{\text{film}}} \sum_{i=1}^{N_{\text{film}}} \left| \frac{\partial \mathcal{U}_{\text{film}}(t_i)}{\partial t} - \frac{dL}{dt}(t_i) \right|^2, \tag{8}$$

where $\mathcal{N}_j$ denotes the PDE operator, $\partial\Omega_j$ the boundary condition operator, and $\mathcal{I}_j$ the initial condition operator for field $j \in \{\text{CV}, \text{AV}, \phi\}$.

The total loss combines these with adaptive weights:

$$\mathcal{L}_{\text{total}} = w_{\text{interior}}\mathcal{L}_{\text{interior}} + w_{\text{boundary}}\mathcal{L}_{\text{boundary}} + w_{\text{initial}}\mathcal{L}_{\text{initial}} + w_{\text{film}}\mathcal{L}_{\text{film}}. \tag{9}$$

3.3 Non-Dimensionalization for Numerical Stability

The PDM involves variables spanning nine orders of magnitude: domain lengths 10^{-9} m, concentrations 10^{-5} mol/m³, and potentials 1 V. This scale disparity causes severe numerical issues including gradient vanishing and floating-point underflow. We implement physics-based non-dimensionalization using characteristic scales:

$$L_c = 1 \times 10^{-9} \text{ m (initial film thickness)}, \tag{10}$$

$$t_c = L_c^2 / D_{CV} \text{ (diffusive time scale)}, \tag{11}$$

$$c_c = 1 \times 10^{-5} \text{ mol/m}^3 \text{ (reference concentration)}, \tag{12}$$

$$\phi_c = RT/F \text{ (thermal voltage)}. \tag{13}$$

This transforms variables to non-dimensional forms:

$$\hat{x} = \frac{x}{L_c}, \quad \hat{t} = \frac{t}{t_c}, \quad \hat{c}_i = \frac{C_i}{c_c}, \quad \hat{\phi} = \frac{\phi}{\phi_c}, \quad \hat{L} = \frac{L}{L_c}. \tag{14}$$

Non-dimensionalization ensures all variables remain O(1), preventing numerical instabilities and extending maximum simulation time from 3,600 seconds (dimensional) to 900,000 seconds (non-dimensional)—a 250× improvement.

3.4 Neural Tangent Kernel-Based Adaptive Weighting

Despite non-dimensionalization, loss components can differ by 4-6 orders of magnitude due to the disparate nature of transport versus electrostatic physics. We implement NTK-based adaptive weighting following Chen et al. [18].

The NTK quantifies each loss component's sensitivity to parameter changes. For loss $\mathcal{L}_j$ with parameters θ, we compute:

$$K_j = J_j J_j^T, \quad \text{where } J_j = \frac{\partial \mathcal{L}_j}{\partial \theta}. \tag{15}$$

The trace of K_j measures overall sensitivity:

$$\text{tr}(K_j) = \sum_{m=1}^{M} \sum_{n=1}^{N} \left(\frac{\partial \mathcal{L}_j(x_n, t_n)}{\partial \theta_m} \right)^2, \tag{16}$$

where M is the number of parameters and N the number of collocation points.

Adaptive weights are computed as:

$$w_j(s) = \frac{N_j}{\text{tr}(K_j(s))} \sum_k \frac{\text{tr}(K_k(s))}{N_k}, \tag{17}$$

ensuring balanced gradients across all physics components. We apply granular weighting to Poisson versus transport equations due to their scale disparity. For computational efficiency, we use statistical sampling with batch size $b_j \geq 25\nu_{X_j}^2$ where ν_{X_j} is the coefficient of variation, updating weights every 100 training steps.

3.5 Sampling Strategy

Training employs mini-batch sampling with uniform random sampling for spatial and temporal coordinates. We use 2048 points for interior/film losses and 1024 for boundary/initial losses. Mini-batch sampling was chosen over uniform grids as it can handle moving boundaries. The number of sampling points was chosen to be the maximum that we could use on our compute. We expect that a denser sampling is better and should be pursued when compute permits.

3.6 The Inclusion of Parameters

A critical aspect of our implementation concerns the careful treatment of parameters such as the applied potential E. If one naively samples E the same way as x, t, the resulting input tensor would contain tuples (x_i, t_i, E_i) where each collocation point has a different applied potential. This is physically meaningless as the electrode maintains a uniform potential.

In this case, we must consider experimental design to understand how to correctly sample E. In an experiment, the experimenter would apply a potential to the electrode then let the film grow, measuring thickness at the final time. Thus we must maintain a consistency per batch, which we can consider as a single experiment data point. This leads to the correct sampling strategy at every collocation point i per batch j of $(x_{i,j}, t_{i,j}, E_j)$

This example demonstrates the need to carefully assess the role of each parameter and sample accordingly. The inclusion of parameters enables generating polarization curves from a single trained model, but requires careful implementation.

3.7 Training Algorithm

Algorithm 1 summarizes the complete training procedure with Adam using a learning rate of 10^{-3}.

Algorithm 1 PINNACLE: PINN Training with NTK-Based Loss Balancing

Input: Networks $\{\mathcal{U}_\phi, \mathcal{U}_{CV}, \mathcal{U}_{AV}, \mathcal{U}_L\}$, Physics operators $\mathcal{P}$
Initialize: Adam optimizer, weights $w_i \leftarrow 1$, step $s \leftarrow 0$
while $s < s_{\max}$ **do**
    Sample collocation points in $[0, \hat{L}(t)] \times [0, \hat{T}] \times [E_{\min}, E_{\max}]$
    Compute predictions and physics residuals
    Calculate losses $\mathcal{L}_{\text{interior}}, \mathcal{L}_{\text{boundary}}, \mathcal{L}_{\text{initial}}, \mathcal{L}_{\text{film}}$
    if $s \bmod 100 = 0$ **then**
        for each loss component $\mathcal{L}_j$ **do**
            Compute NTK trace: $\lambda_j \leftarrow \text{tr}(K_j)/N_j$
        end for
        Update weights via Eq. 17
    end if
    Optimize: $\theta \leftarrow \theta - \eta \nabla_\theta \mathcal{L}_{\text{total}}$
    $s \leftarrow s + 1$
end while
Return: Trained networks

4 Results: Oxide Film Growth Dynamics

4.1 Film Growth Predictions and Voltage Dependence

Figure 1 presents comprehensive predictions of oxide film evolution over 250 hours using NTK-weighted training. The model successfully captures exponential film growth characteristic of passive layer formation, with growth kinetics correctly dependent on applied potential. At 0.1V, minimal growth occurs, this aligns with theoretical expectations from the PDM where low potentials result in negligible defect generation rates.

Higher potentials show progressively faster growth with physically meaningful behavior., Saturation behavior emerges after 150 hours. This saturation corresponds to the establishment of steady-state conditions where defect generation at the metal/film interface balances with defect annihilation at the film/solution interface, a fundamental prediction of the PDM framework. The exponential growth followed by saturation matches the theoretical expectation described by the PDM, where the electric field across the film decreases as thickness increases, reducing the driving force for continued growth.

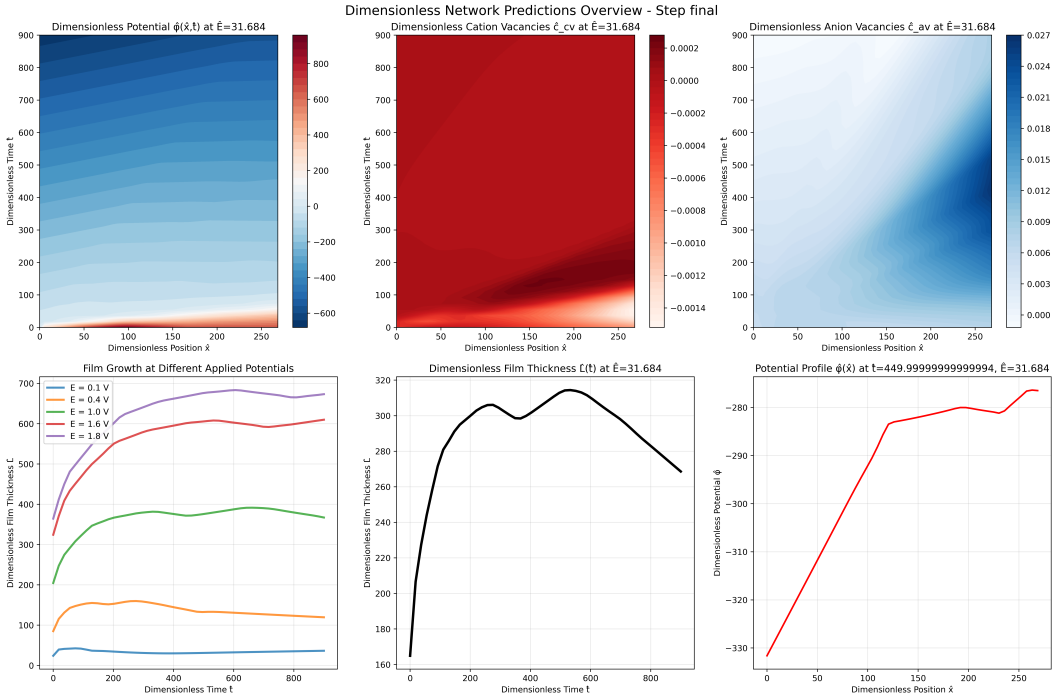

Figure 1: PINN predictions using NTK weighting over 250 hours showing comprehensive oxide film evolution. Top row: (a) electric potential, (b) cation vacancy concentration, (c) anion vacancy concentration. Bottom row: (d) film thickness at multiple potentials (0.1V, 0.4V, 0.8V, 1.2V, 1.5V), (e) detailed growth curve at E=0.8V, (f) potential profile across film at t=125h.

The spatiotemporal evolution reveals complex defect dynamics within the growing film that align with theoretical expectations. Cation vacancy concentrations develop a depletion zone near the metal/film interface while accumulating at the film/solution boundary—consistent with their consumption via reaction R1 at the m/f interface and generation via R3 at the f/s interface. However, we observe unphysical negative concentrations in some depletion regions (Figure 1b), indicating convergence to mathematically valid but physically impossible solutions—a known challenge in physics-informed learning where optimization objectives can conflict with physical constraints.

Anion vacancies show opposite behavior, with higher concentrations near the m/f interface where they are generated (R2) and depletion at the f/s interface where they are consumed (R4). This counter-migration of oppositely charged defects is fundamental to the PDM and demonstrates that the PINN has learned the coupled nature of defect transport under electric fields.

The electric field maintains a quasi-linear profile across the film, as expected from the high-field approximation commonly used in oxide growth models. The slight curvature reflects the space charge contribution from the non-uniform defect distributions, a second-order effect that emerges naturally from solving Poisson's equation coupled with the transport equations.

Comparing to finite elements benchmarks we find that the model significantly overpredicts the film growth at all voltages. Figure 2 shows the PINN predictions vs the FEM predictions at two representative voltages.

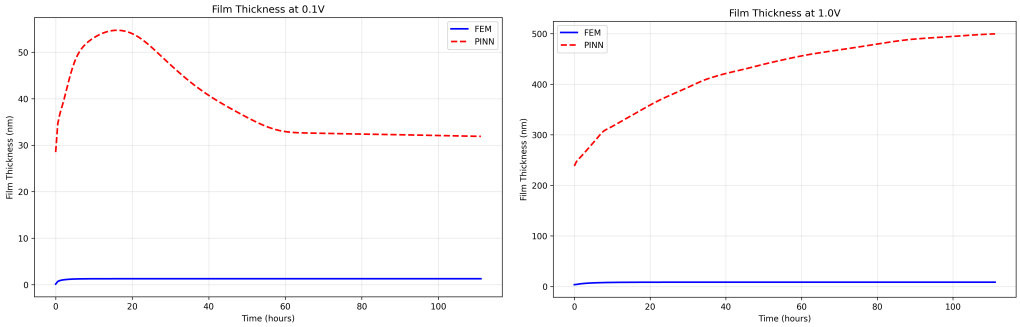

(a) 0.1V (b) 1.0V

Figure 2: PINN vs FEM Predictions

The systemic overpredition coupled with the numerous correct physical phenomena observed support the hypothesis that the model has converged to a solution that is unphysical. Thus we attempted training with a single additional data point to constrain the model. We found that with this extra constraint the model agrees with FEM predictions with excellent accuracy, the improvements and metrics are summarized in Table 1. The predictions are plotted in Figure 3 and indicate that the model is now constrained to the correct scale and are more aligned with the shape of film growth expected with the PDM. This is strong evidence that the key deficit in our PINN is that it is under-constrained and as such, despite learning many of the correct physics converges to an unphysical solution, indicating that future work should focus on enforcing further constraints without compromising optimization.

To demonstrate that improvement is not dependent on careful data selection, we randomly sampled a single point from the FEM solution. This represents a realistic scenario where limited experimental data is available without prior knowledge of optimal measurement locations. We verified robustness by testing N=5 different random selections, with relative error varying by less than 10% across all random data points.

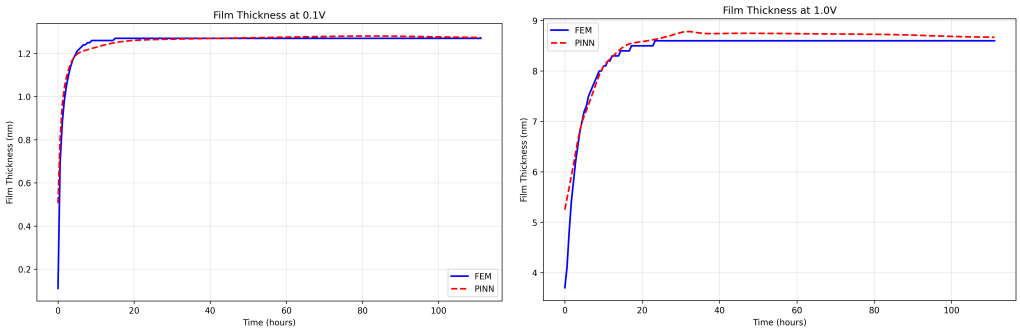

(a) 0.1V (b) 1.0V

Figure 3: Hybrid PINN vs FEM Predictions

Table 1: Comparison of Pure PINN vs Hybrid PINN Performance

Voltage (V)	Pure PINN Error (%)	Hybrid PINN Error (%)	Improvement Factor	Hybrid R^2
0.1	2412	0.32	7537×	0.8975
0.4	4707	0.97	4852×	0.8708
1.0	5708	0.80	7135×	0.9123
1.6	5218	2.18	2393×	0.9428
1.8	5001	0.38	13160×	0.9891

4.2 Addressing Scale Disparities Through Non-Dimensionalization

Figure 4 demonstrates the critical importance of non-dimensionalization. Without it, the dimensional model fails to capture spatial variation in electric potential—the network learns essentially flat profiles due to gradients approaching machine epsilon at nanometer scales. The non-dimensional formulation successfully recovers physically meaningful potential gradients essential for accurate defect transport.

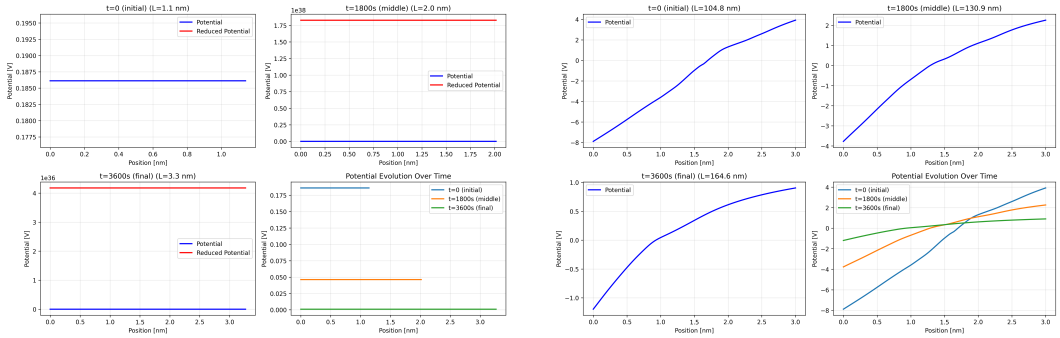

(a) Dimensional model: flat potential

(b) Non-dimensional model: physical gradient

Figure 4: Electric potential profiles: (a) dimensional model, (b) non-dimensional model.

4.3 Loss Component Balancing via NTK

Figure 5 illustrates the effectiveness of NTK-based adaptive weighting. Without weighting, the Poisson equation loss dominates by 4-6 orders of magnitude, preventing the optimizer from learning transport physics. Uniform weighting fails to account for the dynamic nature of training. NTK weighting automatically balances components throughout training, maintaining all losses within one order of magnitude and ensuring coupled physics are learned simultaneously.

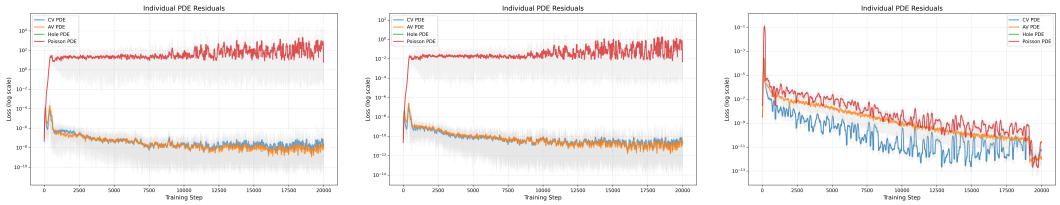

(a) No weighting

(b) Uniform weighting

(c) NTK weighting

Figure 5: PDE loss component evolution: Poisson (red) and transport equations (blue/green). (a) No weighting, (b) Uniform weighting, (c) NTK weighting.

The boundary condition losses exhibit oscillations due to the moving boundary continuously introducing untrained regions. While NTK weighting reduces absolute magnitudes and aligns components, complete elimination of oscillations remains challenging and represents an area for future research.

4.4 Loss Landscape Analysis Reveals Boundary Stiffness

To understand the optimization challenges observed during training, we analyzed the loss landscape structure using filter-normalized visualization. For trained parameters θ^*, we computed:

$$f(\alpha, \beta) = \mathcal{L}(\theta^* + \alpha\eta + \beta\delta), \tag{18}$$

where η, δ are random directions normalized to account for layer-wise scale differences.

Figure 6 reveals a critical finding: the anion vacancy boundary condition at the film/solution interface dominates the total loss landscape, creating a narrow, jagged optimization valley. This landscape topology provides direct evidence for the boundary stiffness we hypothesized based on the oscillating losses. The dominance of this single boundary condition over the entire optimization landscape explains why standard optimizers struggle with moving boundary problems—the gradient signals from boundary constraints overwhelm the interior physics, creating an imbalanced optimization problem that adaptive weighting addressing through minimizing the importance of such stiff constraints, thus losing their character. This observation directly explains the prescience of negative cation concentrations, since mass conservation is generally applied as a boundary constraint.

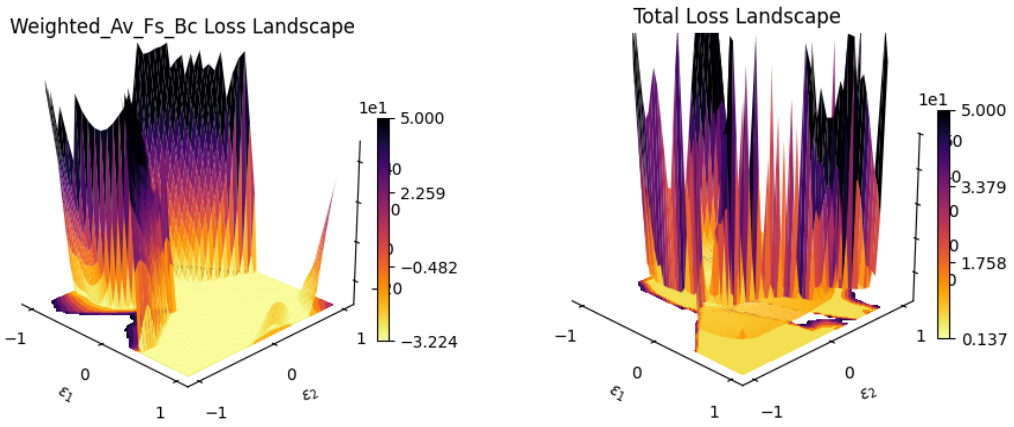

(a) Anion vacancy boundary loss

(b) Total loss landscape

Figure 6: Filter-normalized loss landscapes: (a) anion vacancy boundary loss, (b) total loss landscape.

This analysis demonstrates that boundary condition enforcement in multiphysics PINNs is not merely a weighting problem but a fundamental optimization challenge requiring specialized techniques. The jagged nature of the landscape indicates high sensitivity to parameter perturbations, which leads to a minimization of the respective component by the NTK weighting. Thus for effectively enforcing the character of important constraints while achieving convergence, alternative methods must be explored.

5 Discussion: Successfully Addressed Challenges

Our implementation successfully overcomes two critical obstacles that have limited PINN adoption for realistic multiphysics problems:

Scale Disparity and Numerical Instabilities: The nine-order-of-magnitude span in physical scales represents a fundamental challenge. Traditional input scaling (e.g., log-transformation) fails because it doesn't address the underlying physics. Our physics-based non-dimensionalization using problem-specific characteristic scales ensures all variables and their gradients remain O(1), preventing both overflow/underflow and gradient vanishing. This extends achievable simulation times by 250× and enables learning of spatial variations invisible to dimensional formulations.

Imbalanced Loss Components: Even after non-dimensionalization, the mathematical structure of Poisson versus transport equations creates loss imbalances spanning 4-6 orders of magnitude.

Manual weight tuning is problem-specific and often fails during training dynamics. NTK-based adaptive weighting provides a principled, automatic solution by normalizing gradients based on each component's sensitivity to parameters. This eliminates manual tuning and ensures all physics components contribute equally to optimization.

6 Conclusion

We successfully demonstrate physics-informed neural networks for simulating electrochemical oxide film growth, achieving accurate predictions of oxide film evolution over extended timescales. Through systematic investigation, we identify and address critical challenges that have limited PINN adoption for realistic multiphysics problems. Our key technical contributions include: (1) physics-based non-dimensionalization that extends simulation capability by 250× and prevents numerical instabilities, (2) Neural Tangent Kernel-based adaptive weighting that automatically balances competing physics without manual tuning, (3) diagnostic tools including loss landscape analysis for identifying optimization bottlenecks, and (4) comprehensive guidelines for implementing PINNs in materials science applications. The successful prediction of thin film evolution over 250 hours, capturing voltage-dependent growth kinetics validates the physical consistency of our PINN approach for electrochemical modeling. We quantitatively benchmarked our model against FEM data, finding that our model systemically overpredicts the film thickness, however with the addition of a single data point we were able to achieve sub 1% accuracy across all voltages. Thereby indicating our hypothesis that fully autonomous PINNs require a method that more strongly enforces constrains while still being optimizable or that further constrains must be placed into the mathematical model.

Based on our investigation, we provide actionable guidelines for applying PINNs to multiphysics problems: **Always non-dimensionalize** using physics-based characteristic scales before implementation. This is not optional—dimensional formulations will fail for problems with scale disparities. **Use segregated architectures** for coupled fields. Single networks struggle to learn disparate physics simultaneously. **Include parameters strategically**. Sample global parameters (e.g., applied potential) once per batch, not per collocation point. **Start without weighting** to identify imbalances. If losses differ in magnitude, implement adaptive weighting. **Use NTK weighting** for automatic balancing when adaptive weighting is needed. Update every 50-100 steps to balance computational cost and adaptivity. **Monitor individual components**, not just total loss. Stagnant components indicate optimization issues. **Visualize loss landscapes** when convergence fails. Jagged landscapes indicate poor conditioning; dominated landscapes reveal imbalanced constraints. **Check for pathological solutions** even when losses decrease. Verify physical constraints (positivity, conservation) explicitly. **Start with reduced problems**. Verify on smaller domains/shorter times before scaling up. **Do not overdo network size**: 5-8 layers with 20-50 neurons suffices for most PDEs. Larger networks don't improve accuracy but increase training time.**Follow best practices with activation functions**: Swish outperforms tanh for deep networks. Avoid ReLU for physics problems requiring smooth derivatives. **Be careful about initialization**: Xavier/Glorot initialization with proper scaling for non-dimensional variables but assess performance with and without, we have observed cases where initialization is crucial for successful training and cases where it has caused convergence to pathological solutions. **Introduce spare data** if all above fails.

Future research should pursue several directions. Adressing the remaining challenge of enforcing constraints at moving boundaries and preventing convergence to unphysical solutions remains the primary deficit. These represent fundamental tensions between mathematical optimization and physical constraints that require novel approaches. Advanced optimization strategies like Energy Natural Gradient Descent may enable stronger constraint enforcement via successfully optimizing Augmented Lagrangian loss formulations. Novel architectures such as Kolmogorov-Arnold Networks or physics-constrained designs could inherently respect physical laws. Extension to three-dimensional geometries and inclusion of electronic carriers would enable modeling of more complex passivation phenomena. This work provides a foundation for deploying PINNs in materials science, particularly for problems involving coupled PDEs and moving boundaries characteristic of interfacial phenomena. The methods and guidelines presented are broadly applicable beyond electrochemistry, advancing PINNs toward practical engineering applications in corrosion, catalysis, battery modeling, and materials processing.

References

[1] M. Iannuzzi and G. S. Frankel. The carbon footprint of steel corrosion. *npj Materials Degradation*, 6:101, 2022.

[2] Ahmed Al-Amiery, Wan Nor Roslam Wan Isahak, and Waleed Khalid Al-Azzawi. Sustainable corrosion inhibitors: A key step towards environmentally responsible corrosion control. *Ain Shams Engineering Journal*, 15(5):102672, 2024.

[3] T. Singh and E. Kohn. Harsh Environment Materials. In *Reference Module in Materials Science and Materials Engineering*. Elsevier, January 2016.

[4] Harold J. Fu, Pakpoom Buabthong, Zachary Philip Ifkovits, Weilai Yu, Bruce S. Brunschwig, and Nathan S. Lewis. Catalytic open-circuit passivation by thin metal oxide films of p-si anodes in aqueous alkaline electrolytes. *Energy & Environmental Science*, 15(1):334–345, 2021.

[5] Vincent Maurice and Philippe Marcus. Current developments of nanoscale insight into corrosion protection by passive oxide films. *Current Opinion in Solid State and Materials Science*, 22(4):156–167, 2018.

[6] Digby D. Macdonald. The history of the Point Defect Model for the passive state: A brief review of film growth aspects. *Electrochimica Acta*, 56(4):1761–1772, January 2011.

[7] Antoine Seyeux, Vincent Maurice, and Philippe Marcus. Oxide Film Growth Kinetics on Metals and Alloys: I. Physical Model. *Journal of The Electrochemical Society*, 160(6):C189–C196, 2013.

[8] Kirsten Leistner, Charles Toulemonde, Boubakar Diawara, Antoine Seyeux, and Philippe Marcus. Oxide Film Growth Kinetics on Metals and Alloys: II. Numerical Simulation of Transient Behavior. *Journal of The Electrochemical Society*, 160(6):C197–C205, 2013.

[9] Ingmar Bösing. Modeling electrochemical oxide film growth—passive and transpassive behavior of iron electrodes in halide-free solution. *npj Materials Degradation*, 7(1):53, June 2023.

[10] D.A. Kolotinskii, V.S. Nikolaev, V.V. Stegailov, and A.V. Timofeev. Point Defect Model for the kinetics of oxide film growth on the surface of T91 steel in contact with lead–bismuth eutectic. *Corrosion Science*, 211:110829, 2023.

[11] George R. Engelhardt, Dihao Chen, Chaofang Dong, and Digby D. Macdonald. Estimation of some parameters in the point defect model (PDM) for the passivity of metals. *Journal of The Electrochemical Society*, 171(3):031503, 2024.

[12] C. Bataillon, F. Bouchon, C. Chainais-Hillairet, J. Fuhrmann, E. Hoarau, and R. Touzani. Numerical methods for the simulation of a corrosion model with moving oxide layer. *Journal of Computational Physics*, 231(18):6213–6231, 2012.

[13] Li Sun, Tianyu Zhao, Jie Qiu, Yangting Sun, Kuijiao Li, Haibing Zheng, Yiming Jiang, Yanhui Li, Jin Li, Weihua Li, and Digby D. Macdonald. Point defect model for passivity breakdown on hyper-duplex stainless steel 2707 in solutions containing bromide at different temperatures. *Corrosion Science*, 194:109959, 2022.

[14] M. Raissi, P. Perdikaris, and G. E. Karniadakis. Physics-informed neural networks: A deep learning framework for solving forward and inverse problems involving nonlinear partial differential equations. *Journal of Computational Physics*, 378:686–707, February 2019.

[15] Reyhaneh Taj. Physics-Informed Neural Networks for Electrical Circuit Analysis: Applications in Dielectric Material Modeling, November 2024. arXiv:2411.10483 [cs].

[16] Haotian Chen, Enno Kätelhön, and Richard G Compton. Predicting voltammetry using physics-informed neural networks. *The Journal of Physical Chemistry Letters*, 13(2):536–543, 2022.

[17] Haotian Chen, Enno Kätelhön, and Richard G. Compton. The application of physics-informed neural networks to hydrodynamic voltammetry. *Analyst*, 147:1881–1891, 2022.

[18] Nanxi Chen, Sergio Lucarini, Rujin Ma, Airong Chen, and Chuanjie Cui. PF-PINNs: Physics-informed neural networks for solving coupled allen-cahn and cahn-hilliard phase field equations. *Journal of Computational Physics*, 529:113843, 2025.

[19] Afila Ajithkumar Sophiya, Akarsh K. Nair, Sepehr Maleki, and Senthil K. Krishnababu. A comprehensive analysis of PINNs: Variants, Applications, and Challenges, May 2025. arXiv:2505.22761 [cs].

[20] Runze Sun, Hyogu Jeong, Jiachen Zhao, Yixing Gou, Emilie Sauret, Zirui Li, and Yuantong Gu. A physics-informed neural network framework for multi-physics coupling microfluidic problems. *Computers & Fluids*, 284:106421, November 2024.

[21] Shivprasad Kathane and Shyamprasad Karagadde. A Physics Informed Neural Network (PINN) Methodology for Coupled Moving Boundary PDEs, September 2024. arXiv:2409.10910 [cs].

[22] Ali Al-Safwan, Chao Song, and Umair bin Waheed. Is it time to swish? Comparing activation functions in solving the Helmholtz equation using physics-informed neural networks, October 2021. arXiv:2110.07721 [physics].